

SPLINEGS: LEARNING SMOOTH TRAJECTORIES IN GAUSSIAN SPLATTING FOR DYNAMIC SCENE RE- CONSTRUCTION

Anonymous authors

Paper under double-blind review

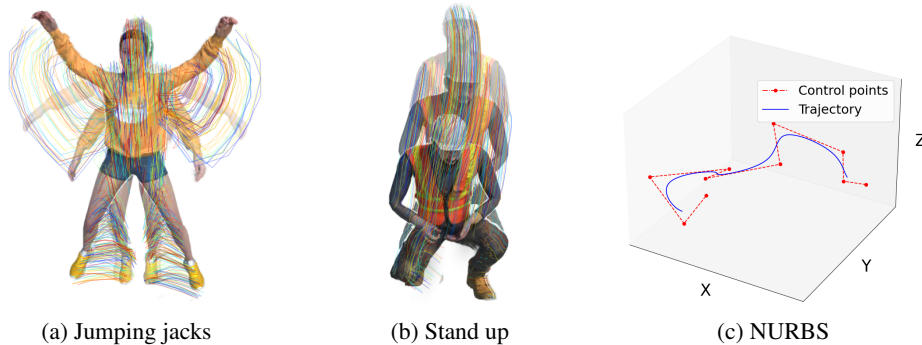


Figure 1: We propose SplineGS, which represents the trajectories in Gaussian splatting using non-uniform rational B-spline (NURBS) to reconstruct dynamic scenes. The learned trajectories are shown with rendering results in (a) and (b). (c) shows an example of a trajectory based on NURBS.

ABSTRACT

Reconstructing complex scenes with deforming objects for novel view synthesis is a challenging task. Recent works have addressed this with 3D Gaussian Splatting, which effectively reconstructs static scenes with high quality in short training time, by adding specialized modules for the deformations of Gaussian blobs. However, designing an effective deformation module that incorporates appropriate spatiotemporal inductive biases still remains unresolved. To address this issue, we propose SplineGS in this paper, which utilizes non-uniform rational B-splines (NURBS), an extension of B-spline, to represent temporally smooth deformation. A set of representative trajectories are learned based on NURBS, and the individual trajectories of Gaussian blobs are represented as linear combinations of these trajectories for spatial smoothness. The weights of the combinations are trained based on a multi-resolution hash table and an MLP, with the positions of the Gaussian blobs as the keys. Thanks to this design, the proposed method does not need any regularizers for trajectories, which enables efficient training. Experiments demonstrate that the proposed method provides competitive performance over the existing methods with much shorter training time.

1 INTRODUCTION

3D reconstruction is a fundamental problem in computer vision and graphics that has been studied for decades. Recently, neural radiance fields (NeRF) (Mildenhall et al., 2020) have achieved a remarkable breakthrough in novel view synthesis (NVS) based on implicit representations. However, NeRF still suffered from limited performance and, especially, slow training times, prompting the development of various subsequent methods (Yu et al., 2021; Fridovich-Keil et al., 2022; Chen et al., 2022; Barron et al., 2021; 2023). Recently, 3D Gaussian Splatting (3D-GS) (Kerbl et al., 2023) has emerged as a successful alternative by representing scenes based on 3D Gaussian blobs and employing a differentiable tile rasterizer, resulting in fast, high-quality rendering and thus reduced training time.

054 Despite the success of 3D-GS in static scenes, applying it to dynamic scenes with deforming objects
 055 remains a challenging task due to the difficulty in modeling effective trajectory representations. Re-
 056 cent works have proposed various methods to model the trajectories of 3D Gaussian blobs over
 057 time to reconstruct dynamic scenes. Approaches that express deformations based on neural rep-
 058 resentations (Yang et al., 2024b; Wu et al., 2024) optimize canonical 3D Gaussian blobs as well
 059 as a neural module to predict temporal deformations. Neural representations in these approaches,
 060 however, do not provide enough inductive biases for deformations, and additional training mecha-
 061 nisms or smoothness regularizers are utilized to handle these. Another approach directly optimizes
 062 4D Gaussian blobs (Yang et al., 2024a; Duan et al., 2024), which introduces challenges in optimiza-
 063 tion due to the higher dimensionality (4D). This results in reconstruction artifacts, such as floating
 064 objects that do not align correctly with the scene. Even though these previous works have shown
 065 impressive performance, the trajectory representations they use impose some limitations on either
 066 performance, convergence speed, or both.

067 In this paper, we propose a novel method, i.e., SplineGS, that models the trajectories of 3D Gaus-
 068 sian blobs as temporally smooth representations based on non-uniform rational B-splines (NURBS)
 069 (Piegl & Tiller, 2012), an extension of B-splines (De Boor, 2001), to reconstruct dynamic scenes.
 070 NURBS can represent continuous and smooth trajectories, similar to B-splines, while allowing for
 071 more flexible and finer adjustments. Our approach specifically obtains a set of representative trajec-
 072 tories for both positions and rotations through NURBS, of which the parameters are learned during
 073 the training. To ensure spatial smoothness, the individual trajectory of each Gaussian blob is ex-
 074 pressed as a linear combination of these representative trajectories. Inspired by Müller et al. (2022),
 075 the weights for these combinations are obtained using a multi-resolution hash table and a multi-layer
 076 perceptron (MLP), where the average position of each Gaussian blob serves as the key. The NURBS
 077 representation and the linear combination strategy act as implicit regularizers embedded within the
 078 structure. Based on this smooth representation, our approach achieves high-fidelity rendering and
 079 fast training time without relying on any explicit smoothness regularizers, making it efficient for
 complex dynamic scenes.

080 We evaluated the proposed method on two dynamic-scene datasets, i.e., D-NeRF (Pumarola et al.,
 081 2021) and Neu3D (Li et al., 2022). Experimental results demonstrate that the proposed method
 082 achieves highly competitive performance, even with shorter training time.

083 Our contributions are summarized as follows:

- 084
- 085 • We propose temporally smooth representations for the trajectories of Gaussian blobs based
 086 on NURBS.
- 087 • We enforce spatial smoothness by introducing a low-rank assumption for the trajectories.
 088 Each Gaussian blob’s trajectory is modeled as a weighted sum of representative trajectories,
 089 where the weights are learned by a multi-resolution hash table and an MLP. This eliminates
 090 the need for a separate smoothness regularizer.
- 091 • The proposed smooth representation exhibits physically plausible trajectories, which leads
 092 to high-fidelity rendering and fast training times.

093 2 RELATED WORK

094 In this section, we briefly review the NeRF-based methods for dynamic scenes. Following this,
 095 we introduce the original 3D-GS for static scenes and the methods that extend 3D-GS to dynamic
 096 scenes.

097 2.1 NEURAL RADIANCE FIELDS FOR DYNAMIC SCENES

098 In recent years, NeRF-based methods have gained significant attention for solving the NVS prob-
 099 lem of static scenes. This surge in interest was largely due to the impressive performance of vanilla
 100 NeRF, which has inspired subsequent research efforts aimed at improving memory usage, training
 101 speed, rendering quality, and rendering speed. In addition, many attempts have been made to ex-
 102 tend it to dynamic scenes. D-NeRF (Pumarola et al., 2021) and Nerfies (Park et al., 2021a) utilize
 103 the coordinates in a canonical space and time embedding vectors as inputs to the MLP to compute
 104 the deformations. HyperNeRF (Park et al., 2021b) further enhanced this approach by embedding a

108 template NeRF in a higher-dimensional space to better capture topological changes. However, these
 109 methods often suffer from inefficiency in rendering due to the high number of queries required for
 110 the MLP. Spline-NeRF (Knodt, 2022) takes all sampled points along a ray as inputs to an MLP,
 111 which then outputs control points for Bézier curves. However, it is difficult to represent a complex
 112 trajectory, e.g., one that has many temporally local changes, based on a Bézier curve. A Bézier curve
 113 is a global representation, i.e., changes in some control points affect the entire shape of the curve.
 114 Accordingly, it becomes challenging to apply this method to long video sequences. On the other
 115 hand, *K*-Planes (Fridovich-Keil et al., 2023) and HexPlane (Cao & Johnson, 2023) represented
 116 4D spacetime by combining multiple 2D planes, improving speed and interpretability through ex-
 117 plicit representations. Nevertheless, the complexity of dynamic scenes and the inherent limitations
 118 of ray-casting-based rendering prevent these methods from achieving high-fidelity and high-speed
 119 rendering required for practical applications.

120 2.2 3D GAUSSIAN SPLATTING FOR DYNAMIC SCENES

122 Recently, 3D-GS has emerged as a successful solution for reconstructing static scenes, achieving
 123 high-fidelity rendering, fast rendering speed, and fast training time. 3D-GS directly optimizes the
 124 means, scales, rotations, opacities, and colors of 3D Gaussian blobs that compose a static scene
 125 using a differentiable tile-based rasterizer. Inspired by this success, research efforts have begun to
 126 explore the use of 3D-GS for reconstructing dynamic scenes (Wu et al., 2024; Yang et al., 2024b;
 127 Huang et al., 2024; Yang et al., 2024a; Duan et al., 2024; Luiten et al., 2024; Bae et al., 2024). For
 128 example, 4D-GS (Wu et al., 2024) introduces a spatial-temporal structure encoder, which is com-
 129 posed of a multi-resolution HexPlane and a tiny MLP, along with additional MLPs to compute the
 130 deformations. In another study (Yang et al., 2024b), purely implicit networks, i.e., MLPs, are used
 131 to compute temporal deformations. In SC-GS (Huang et al., 2024), anchor-based spatial warping
 132 and MLPs are learned to represent deformations of the overall 3D Gaussian blobs. However, these
 133 approaches rely on neural representations, which do not provide enough inductive biases, so ad-
 134 ditional training mechanisms or smoothness regularizers are utilized. On the other hand, there are
 135 methods (Yang et al., 2024a; Duan et al., 2024) that directly optimize 4D Gaussian blobs. While
 136 this approach allows for a flexible representation of complex dynamic scenes, it also introduces
 137 challenges in optimization due to the increased dimensionality (4D). These challenges can lead to
 138 reconstruction artifacts, such as floating objects, and achieving high-quality reconstructions requires
 139 additional regularizers or extended training time. Alternatively, polynomial and Fourier bases (Lin
 140 et al., 2024) can also be used to represent trajectories. However, since this approach must utilize all
 141 the bases to calculate deformation at a specific time, it can be more challenging to model temporally
 142 local deformations and the computational cost can increase significantly when reconstructing long
 143 video sequences.

144 3 THE PROPOSED METHOD

146 In this section, we propose SplineGS, which represents deformations based on spatiotemporally
 147 smooth representations. First, we review 3D Gaussian Splatting in Section 3.1. In Section 3.2, we
 148 introduce the B-spline (non-uniform rational B-splines (NURBS), specifically) representations for
 149 the trajectories of Gaussian blobs. Then, in Section 3.3, a multi-resolution hash table and an MLP
 150 are utilized to enforce spatial smoothness based on linear combinations of representative trajectories.
 151 Finally, in Section 3.4, we describe the objective function for optimization. The pipeline of SplineGS
 152 is illustrated in Figure 2.

153 3.1 PRELIMINARY: 3D GAUSSIAN SPLATTING

155 3D-GS Kerbl et al. (2023) reconstructs a static scene by directly optimizing the means, covariance
 156 matrices, opacities, and colors of 3D Gaussian blobs. Given N Gaussian blobs, the shape of each
 157 Gaussian is represented by its mean x_i and covariance matrix Σ_i :

$$158 G_i(\mu) = e^{-\frac{1}{2}(\mu - \mu_i)^T \Sigma_i^{-1} (\mu - \mu_i)}, \quad (1)$$

159 The covariance matrix must be positive semi-definite, and this is ensured during optimization by
 160 separately optimizing the corresponding scales and rotations, i.e., S_i and R_i :

$$161 \Sigma_i = R_i S_i S_i^T R_i^T. \quad (2)$$

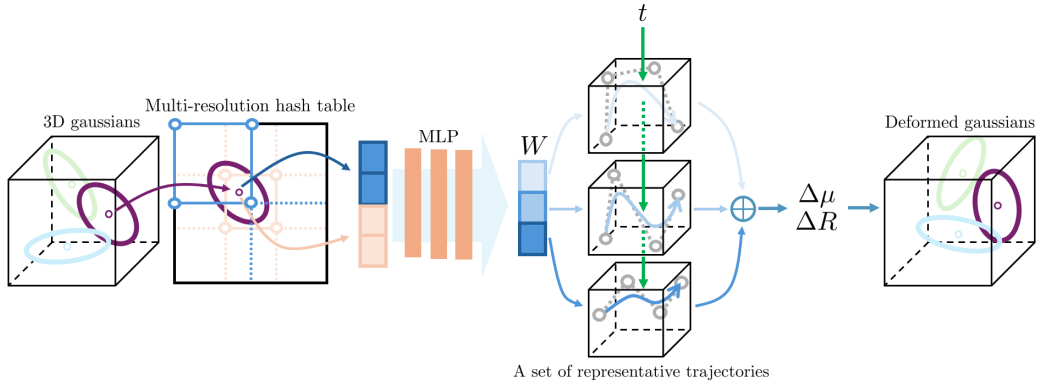


Figure 2: **The pipeline of the proposed method.** For each given 3D Gaussian blob, the positions normalized into the range of $[0, 1]^3$ are used as keys for the multi-resolution hash table. The features derived from the position are then mapped to weights via an MLP for the linear combination of representative trajectories. Meanwhile, the relative positions and rotations of the representative trajectories at time t are calculated based on NURBS. Finally, the deformation of each Gaussian blob is obtained by a linear combination.

To render the 3D Gaussian blobs in the scene onto a 2D image space, the 2D covariance matrix Σ'_i in camera coordinates is derived using a given camera extrinsic transform W and the Jacobian of the affine approximation matrix J (Zwicker et al., 2001):

$$\Sigma'_i = JW\Sigma_iW^TJ. \quad (3)$$

Afterward, the pixel’s color C is computed by blending N' -ordered blobs that overlap the pixel.

$$C = \sum_{k=1}^{N'} c_{i_k} \alpha_{i_k} \prod_{j=1}^{k-1} (1 - \alpha_{i_j}). \quad (4)$$

where $\{i_k\}$ represents the indices of the overlapping blobs and c_i denotes the color of each blob. α_i is determined by evaluating the 2D Gaussian with covariance Σ'_i and multiplying it by a learned per-point opacity.

3.2 TRAJECTORY REPRESENTATIONS BASED ON B-SPLINES

We employ non-uniform rational B-splines (NURBS) (Piegl & Tiller, 2012) to represent smooth trajectories over time. Here, we first explain the basic formulation based on B-splines, and then extend it to NURBS.

B-splines. B-splines (De Boor, 2001) are defined as a set of piecewise polynomial functions, where each polynomial has a specific degree denoted as p . These polynomial functions are connected continuously at specific points called knots, represented by $t_0, t_1, \dots, t_{p+M+1}$. Here, M is the number of control points which will be defined later. The curve’s shape is determined as a linear combination of control points and their corresponding basis functions. When $p = 0$, the influence of the i -th control point at a given time is described by the basis function as follows:

$$B_{i,0}(t) := \begin{cases} 1 & \text{if } t_i \leq t < t_{i+1}, \\ 0 & \text{otherwise.} \end{cases} \quad (5)$$

The higher-degree B-splines, starting from $p = 0$, can be defined using the Cox-de Boor recursion formula:

$$B_{i,p}(t) := \frac{t - t_i}{t_{i+p} - t_i} B_{i,p-1}(t) + \frac{t_{i+p+1} - t}{t_{i+p+1} - t_{i+1}} B_{i+1,p-1}(t). \quad (6)$$

Once the basis functions are determined, the position at any given time t is computed as a linear combination of the control points, with these functions acting as weights.

$$S(t, P) = \sum_{i=0}^n B_{i,p}(t) P_i \quad (7)$$

where $S(t, P)$ denotes the position of the B-spline curve at time t and $P = \{P_i\}$ are the control points that define the curve’s shape.

Non-uniform rational B-splines. To represent more complex trajectories, the trajectory of a Gaussian blob can be modeled using non-uniform rational B-spline (NURBS), an extension of B-splines. NURBS allows for finer controls of the trajectory by incorporating an additional weight for each control point, and a NURBS curve is expressed as follows:

$$S(t, w, P) = \frac{\sum_{i=0}^M B_{i,p}(t)w_i P_i}{\sum_{i=0}^M B_{i,p}(t)w_i} \quad (8)$$

where w_i denotes the weight associated with the control point P_i . Here, assigning uniform weights makes it equivalent to plain B-splines. Assigning non-uniform weights allows for more flexible adjustment over the control points that represent complex motion. Additionally, during simpler motions, simplification can be encouraged by adopting low weights.

In this paper, we utilize NURBS to represent the trajectory of a Gaussian blob (i.e., translation and rotation), and P and w_i are regarded as learnable parameters. Note that the NURBS trajectories in this paper are defined as the differences from the canonical (or static) positions or rotations. In other words, the trajectories must be combined with the static positions or rotations before use. The static positions and rotations of blobs are separate learnable parameters in the proposed method, along with colors defined as spherical harmonics, opacities, and scales. The degree p and the number of control points M are hyperparameters, and the number of knots is determined as $p + M + 1$. The locations of knots are defined as equally spaced points in the entire time frame.

3.3 BLENDING REPRESENTATIVE TRAJECTORIES FOR SPATIAL SMOOTHNESS

Optimizing B-splines for each 3D Gaussian blob separately has several drawbacks: First of all, it requires a large memory space and can increase the overall complexity of optimization. More importantly, spatial smoothness, which is expected in between the trajectories in proximity, is not guaranteed. To resolve these issues all at once, we instead represent the individual trajectories as weighted sums of a few representative trajectories, which only are defined based on NURBS. The weights for these sums are obtained by a multi-resolution hash table and an MLP, which is inspired by instantNGP (Müller et al., 2022), using the position of each Gaussian blob as the key:

$$\beta_j = \tanh(\text{MLP}(\text{Hash}(\mu_j))) \quad \text{for } j = 1, 2, \dots, N \quad (9)$$

where $\mu_j \in \mathbb{R}^3$ represents the center position of the j -th blob, N denotes the number of Gaussians, $\beta_j \in \mathbb{R}^L$ is the weight vector of the corresponding Gaussian blob, and L is the number of representative trajectories. We apply \tanh to the weights to limit their range to $[-1, 1]$. Note here that we do not use any explicit spatial-proximity-based operations, such as kernel regression or K -nearest neighbors (Huang et al., 2024), and instead learn the weights implicitly by the hash table and MLP. This can effectively prevent the overall computational complexity of the training procedure from increasing.

After obtaining the weights, the positions and rotations of the representative trajectories at time t , calculated based on NURBS, are combined by the weights. The weighted sum operation is applied in the original 3D space for the positions, while it is applied to the axis-angle representations for the rotations and then converted to quaternions.

$$\Delta\mu_j(t) = \sum_{k=0}^{L-1} \beta_{j,k} \cdot S(t, w_k, P_k^{\text{pos}}), \quad (10)$$

$$\Delta R_j(t) = \mathcal{Q} \left(\sum_{k=0}^{L-1} \beta_{j,k} \cdot S(t, w_k, P_k^{\text{rot}}) \right), \quad (11)$$

$$\mu_j(t) = \mu_j + \Delta\mu_j(t), \quad (12)$$

$$R_j(t) = R_j \cdot \Delta R_j(t), \quad (13)$$

where $P_k^{\text{pos}} \in \mathbb{R}^{M \times 3}$ and $P_k^{\text{rot}} \in \mathbb{R}^{M \times 3}$ represent the control points for positions and rotations, respectively, for the k -th representative trajectory, and $w_k \in \mathbb{R}^M$ denotes the corresponding weights

(of the control points) in NURBS. \mathcal{Q} denotes the axis-angle-to-quaternion conversion. The position and rotation from the first two equations are relative ones (from the static position and rotation, respectively), so they are combined with the static ones in the last two equations. The above technique effectively suppresses unwanted, abrupt spatial variations and promotes gradual changes. Accordingly, the proposed method can ensure spatial smoothness without increasing the overall computational complexity, and also has compact feature representations.

3.4 OPTIMIZATION

The proposed method incorporates the above spline module on top of the original 3D-GS to estimate deformations. This process is performed end-to-end, and we term this method SplineGS.

Reconstruction loss. The reconstruction loss is defined as the difference between the ground truth image and the rendered image. Similar to 3D-GS (Kerbl et al., 2023), we include both \mathcal{L}_1 and \mathcal{L}_{D-SSIM} :

$$\mathcal{L}_{\text{recon}} = (1 - \lambda)\mathcal{L}_1 + \lambda\mathcal{L}_{D-SSIM} \quad (14)$$

where λ is a predefined weight.

Sparsity. In complex scenes, particularly with real-world datasets, the diversity and complexity of object structures lead to an increased number of Gaussian blobs to represent fine details. This, on the other hand, generates artifacts, such as floating objects, and increases memory usage. To prevent the creation of unnecessary 3D Gaussian blobs, we add L1 regularization on the opacity values:

$$\mathcal{L} = \mathcal{L}_{\text{recon}} + \lambda_o \sum_{j=1}^N |o_j| \quad (15)$$

where λ_o is also a predefined weight and o_j is the opacity of the j th blob.

4 EXPERIMENTS

In this section, we evaluate SplineGS on the D-NeRF (Pumarola et al., 2021) and Neu3D (Li et al., 2022) datasets. Performance was measured using PSNR, D-SSIM, training time, and FPS, and compared with existing NeRF-based and 3D-GS-based methods.

4.1 DATASETS

D-NeRF dataset. The D-NeRF dataset consists of monocular video frames with well-aligned camera poses. This synthetic dataset includes 8 scenes: *bouncingballs*, *hellwarrior*, *hook*, *jumpingjacks*, *mutant*, *standup*, *trex* and *lego*, each of which contains between 50 and 200 training images and 20 test images. The experiments were conducted at a resolution of 800×800.

Neu3D dataset. This is a real-world dataset that includes 6 scenes: *coffee_martini*, *cook_spinach*, *cut_roasted_beef*, *sear_steak*, *flame_steak* and *flame_salmon*. Each scene, except for *flame_salmon*, was recorded for 10 seconds at 30 fps using 15 to 20 fixed cameras, with one camera designated as the test view. The experiments were conducted at half resolution, i.e., 1352×1014. We did not use *flame_salmon*, which consists of 1200 frames, in the experiments, following the practices of many existing methods (Guo et al., 2024; Liu et al., 2024; Lu et al., 2024).

4.2 IMPLEMENTATION DETAILS

We implemented SplineGS by integrating the proposed spline-based deformation module, implemented using PyTorch (Paszke et al., 2019), with the original 3D-GS (Kerbl et al., 2023). For the D-NeRF dataset, we randomly sample 100,000 points within a 3D space, where each axis ranges from -1.3 to 1.3, to initialize 3D Gaussian blobs. For the Neu3D dataset, the initial set of 3D Gaussians is obtained by calculating structure-from-motion (Schönberger & Frahm, 2016) for the first frames of each video and downsampling the results. The detailed settings for this were identical to those in 4D-GS (Wu et al., 2024). The initialization of scales, rotations, colors, opacities, and their respective learning rates follows the 3D-GS. Similarly, during training, we adopt the clone and split strategies with a threshold of 2×10^{-4} , as in 3D-GS. For the D-NeRF dataset, we also utilized the

Table 1: **Quantitative comparison for the D-NeRF dataset.** We compared our method to existing methods on 800×800 resolution test images. Here, “40K” and “80K” in the parentheses indicate the numbers of training iterations. The asterisks (*) indicate that the results were adopted from the 4D-GS paper (Wu et al., 2024), while the daggers (†) indicate that those were from the original papers. All the other results were reproduced in our experiments. The average PSNR and SSIM are measured across all scenes, with some cells highlighted to represent the **best**, **second best**, and **third best**. Additionally, we report the average training time and rendering speed in frames per second (FPS) for each method.

Method	PSNR↑	SSIM↑	Training time↓	FPS↑
<i>K</i> -Planes* (Fridovich-Keil et al., 2023)	30.67	0.9672	52 mins	0.97
HexPlane* (Cao & Johnson, 2023)	31.02	0.9680	11 mins	2.5
TiNeuVox* (Fang et al., 2022)	31.35	0.9613	28 mins	1.5
D-3DGS.† (Yang et al., 2024b)	38.50	0.9857	22 mins	70
4D-GS* (Wu et al., 2024)	34.06	0.9787	13 mins	62
4DGS (Yang et al., 2024a)	32.87	0.9649	7.5 hours	135
CoGS† (Yu et al., 2024)	37.90	0.9842	-	-
CompDynGS† (Katsumata et al., 2024)	33.21	0.9770	8 mins	150
SC-GS (Huang et al., 2024)	39.53	0.9906	1.1 hours	111
SplineGS (40K)	39.11	0.9866	17 mins	188
SplineGS (80K)	39.44	0.9868	35 mins	188



Figure 3: **Qualitative results for the D-NeRF dataset.** We present the rendering results of various methods, including ours, with the ground truth (GT) for *standup* scene in the D-NeRF dataset. Additional rendering results for other scenes are provided in the appendix.

repeated opacity reset suggested in 3D-GS. The training process begins with initial 3K iterations of static 3D-GS training (ignoring any deformations), followed by an end-to-end training with the proposed spline module.

For the spline module, the number of control points (per trajectory) was set as one for every four to eight frames collected from a single camera. These control points were initialized with a normal distribution with a standard deviation 10^{-5} . The number of representative trajectories was set to either 64 or 128, depending on the dataset. The initial learning rate for the control points was set to 10^{-3} for the D-NeRF dataset and 5×10^{-3} for the Neu3D dataset, with a decay factor of 0.99 for every 100 iterations. Similarly, the learning rate of w_k was initialized to 10^{-3} for the D-NeRF dataset and 5×10^{-4} for the Neu3D dataset, and also decayed by a factor of 0.99 for every 100 iterations. The multi-resolution hash table and MLP were implemented using *tiny-cuda-nn* (Müller, 2021), with 16 levels and 4 features per level. The maximum table size parameter, base resolution, and per-level scale were set to 19, 8, and 2, respectively, for the D-NeRF dataset and 15, 16, and 1.5, respectively, for the Neu3D dataset. The MLP consisted of 4 hidden layers with hidden dimensions of 128 for all the layers. The optimization of the spline module, like 3D-GS, was performed using Adam (Kingma, 2014).

The performance of SplineGS was evaluated after 40K and 80K iterations on the D-NeRF dataset, and 20K and 40K iterations on the DyNeRF dataset, with results averaged over three runs. All the experiments were conducted on a single Nvidia Geforce RTX 3090.

Table 2: **Quantitative comparison for the Neu3D dataset.** We compared our method with existing methods on 1352×1014 resolution test images. Here, “20K” and “40K” in the parentheses indicate the numbers of training iterations. The conventions for typographical marks and color codes are generally identical to Table 1. We measured the average PSNR and SSIM across all scenes except *flame_salmon*, following the practice of many existing works (Guo et al., 2024; Liu et al., 2024; Lu et al., 2024). The double dagger (‡) denotes that the mean values were calculated across all scenes in the respective work.

Method	PSNR↑	SSIM↑	Training time↓	FPS↑
NeRFPlayer* (Song et al., 2023)	32.12	0.9206	5.5 hours	0.045
<i>K</i> -Planes* (Fridovich-Keil et al., 2023)	31.86	0.9658	1.8 hours	0.23
4D-GS* (Wu et al., 2024)	31.54	0.9444	40 mins	30
Gaussian-Flow‡ (Lin et al., 2024)	32.00	0.9700	42 mins	-
4DGS† (Yang et al., 2024a)	32.53	-	-	114
STG† (Li et al., 2024)	32.57	0.9740	42 mins×6	140
SplineGS (20K)	32.52	0.9484	27 mins	76
SplineGS (40K)	32.60	0.9496	55 mins	76

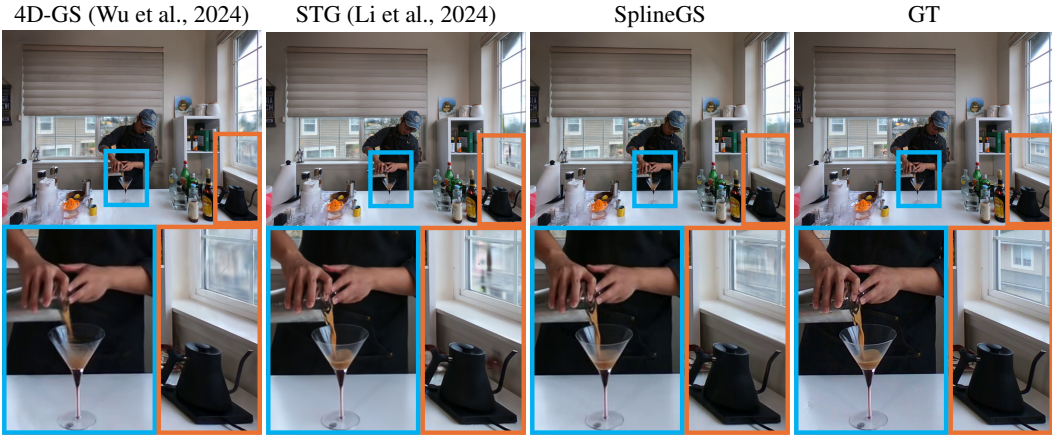


Figure 4: **Qualitative results for the Neu3D dataset.** We present the rendering results of various methods, including ours, and the ground truth (GT) for *coffee_martini* in the Neu3D dataset. We also provide zoomed-in results in the second row of the figure. Additional results for other scenes are provided in the appendix.

4.3 RESULTS

Results on synthetic scenes. Here, we compared the proposed model with various NeRF-based methods: *K*-Planes (Fridovich-Keil et al., 2023), HexPlane (Cao & Johnson, 2023), and TiNeuVox (Fang et al., 2022); as well as 3D-GS-based methods: Yang et al. (2024b), 4D-GS (Wu et al., 2024), 4DGS (Yang et al., 2024a), CoGS (Yu et al., 2024), Katsumata et al. (2024), SC-GS (Huang et al., 2024)) on the D-NeRF dataset. A quantitative evaluation of average PSNR, SSIM, training time, and FPS is shown in Table 1. Here, the proposed method ranks second best, but with significantly shorter training time compared to the best performing one while having a very small performance gap. This observation suggests that the proposed spline representation is well suited for dynamic scene reconstruction. More detailed qualitative and quantitative comparisons for each scene are provided in the appendix. Figure 3 shows the qualitative comparison for *standup*. Here, we can confirm that the proposed method yields more accurate rendering compared to the existing methods.

Results on Neu3D. For the Neu3D dataset, we compared with the following NeRF-based methods: NeRFPlayer (Kerbl et al., 2023), *K*-Planes Fridovich-Keil et al. (2023); as well as 3D-GS-based methods: 4D-GS (Wu et al., 2024), 4DGS (Yang et al., 2024a) and STG (Li et al., 2024). Table 2 presents the quantitative comparison. For this dataset, the proposed method achieves the best average

Table 3: **Effect of the degree of NURBS.** We quantitatively evaluated the effect of the degree of NURBS in our method on synthetic and real-world scenes.

Degree p	Bouncing Balls		Hook		Coffee Martini		Sear Steak	
	PSNR \uparrow	SSIM \uparrow	PSNR \uparrow	SSIM \uparrow	PSNR \uparrow	SSIM \uparrow	PSNR \uparrow	SSIM \uparrow
$p = 0$	36.03	0.9915	28.43	0.9441	28.42	0.9127	33.61	0.9606
$p = 1$	40.93	0.9951	38.09	0.9879	28.56	0.9154	33.49	0.9610
$p = 2$	41.26	0.9954	38.59	0.9890	29.01	0.9178	33.66	0.9621
$p = 3$	41.81	0.9956	38.71	0.9891	29.26	0.9189	33.82	0.9624
$p = 4$	39.97	0.9946	26.98	0.9311	28.64	0.9184	33.59	0.9621

Table 4: **Ablation study.** We quantitatively evaluated the effect of different components of the proposed method on synthetic and real-world scenes.

Method	Bouncing Balls		Hook		Coffee Martini		Sear Steak	
	PSNR \uparrow	SSIM \uparrow	PSNR \uparrow	SSIM \uparrow	PSNR \uparrow	SSIM \uparrow	PSNR \uparrow	SSIM \uparrow
w/o hash	41.20	0.9949	36.39	0.9813	27.98	0.9041	30.87	0.9473
w/o MLP	38.33	0.9927	37.80	0.9879	28.80	0.9160	33.19	0.9605
w/o NURBS	39.83	0.9944	26.82	0.9306	28.85	0.9181	32.08	0.9559
proposed	41.81	0.9956	38.71	0.9891	29.26	0.9189	33.82	0.9624

PSNR after 40K iterations. Moreover, the proposed method always achieves better performance per training time than the existing methods. Here, STG divides the entire video frames (300 frames) into 6 parts (50 frames each) and then processes them separately, which is why the training time is described as “42 mins \times 6”. Again, the detailed results for each scene are provided in the appendix. Figure 4 shows the qualitative comparisons on the *coffee_martini* scene. Here, the proposed method provides crisper details for the *coffee_martini*.

SplineGS concentrates on the temporal changes of position and rotation, without modeling those of density and color unlike some recent methods (Yang et al., 2024a; Li et al., 2024; Lin et al., 2024). Nevertheless, it achieves high-fidelity rendering and fast convergence, which suggests that the proposed spline representation provides a better alternative for modeling deformations.

4.4 ANALYSES AND ABLATION STUDY

Effect of the degree of NURBS. In NURBS, the value of a trajectory at a specific time instance is influenced by surrounding $p + 1$ control points. Accordingly, as the degree increases, the curve becomes less sensitive to the changes in control points, which makes the trajectory smoother but also increases the computational cost. Table 3 shows the performance variations according to the changes in the degree for *bouncing balls*, *hook*, *coffee_martini*, *sear_steak*. The results indicate that $p = 3$ generally provides optimal performance for dynamic scenes.

Ablation study on the module components. We provide an ablation study on the spline module in Table 4. Here, “w/o hash” indicates that the multiresolution hash table was replaced with a positional encoding $\gamma(p) = (\sin(2^k \pi p), \cos(2^k \pi p))_{k=0}^{L-1}$ with $L = 10$. In this case, performance generally decreases except for *bouncingballs*, which contains less complex motions. In the case of “w/o MLP”, the hash table directly outputted the weights for the linear combination, which generally resulted in lower performance. In the “w/o NURBS” scenario, the MLP directly outputs the values of a trajectory given a time instance t : the features generated by the hash table are concatenated with the positional encoding (with $L = 6$) of t , and then go through the MLP to output the values. This variation leads to lower performance, which suggests that the neural representation alone lacks sufficient spatiotemporal inductive biases.

5 CONCLUSION

We proposed SplineGS, which utilizes a smooth representation in both space and time for the trajectory of each 3D Gaussian blob, to reconstruct dynamic scenes. Thanks to this representation, the proposed method achieves state-of-the-art or at least competitive performance without the need for a regularizer on the trajectories. The proposed spline representation is an explicit representation, in that the NURBS directly represents the trajectories of Gaussian blobs. This is well suited for dynamic scene reconstruction, providing fast convergence. The proposed model only handles deformations in positions and rotations, so it has limitations in reconstructing objects that appear or disappear in scenes, as well as objects with rapidly changing colors due to lighting variations. Incorporating advanced light reflections and accounting for changes in blob density will be explored in future work.

REFERENCES

- Jeongmin Bae, Seoha Kim, Youngsik Yun, Hahyun Lee, Gun Bang, and Youngjung Uh. Per-gaussian embedding-based deformation for deformable 3d gaussian splatting. In *European Conference on Computer Vision (ECCV)*, 2024.
- Jonathan T. Barron, Ben Mildenhall, Matthew Tancik, Peter Hedman, Ricardo Martin-Brualla, and Pratul P. Srinivasan. Mip-nerf: A multiscale representation for anti-aliasing neural radiance fields. *ICCV*, 2021.
- Jonathan T. Barron, Ben Mildenhall, Dor Verbin, Pratul P. Srinivasan, and Peter Hedman. Zip-nerf: Anti-aliased grid-based neural radiance fields. *ICCV*, 2023.
- Ang Cao and Justin Johnson. Hexplane: A fast representation for dynamic scenes. In *Proceedings of the IEEE/CVF Conference on Computer Vision and Pattern Recognition*, pp. 130–141, 2023.
- Anpei Chen, Zexiang Xu, Andreas Geiger, Jingyi Yu, and Hao Su. Tensorf: Tensorial radiance fields. In *European Conference on Computer Vision (ECCV)*, 2022.
- Devikalyan Das, Christopher Wewer, Raza Yunus, Eddy Ilg, and Jan Eric Lenssen. Neural parametric gaussians for monocular non-rigid object reconstruction. In *Proceedings of the IEEE/CVF Conference on Computer Vision and Pattern Recognition*, pp. 10715–10725, 2024.
- Carl De Boor. *A practical guide to splines; rev. ed.* Applied mathematical sciences. Springer, Berlin, 2001. URL <https://cds.cern.ch/record/1428148>.
- Yuanxing Duan, Fangyin Wei, Qiyu Dai, Yuhang He, Wenzheng Chen, and Baoquan Chen. 4d-rotor gaussian splatting: Towards efficient novel view synthesis for dynamic scenes. In *ACM SIGGRAPH 2024 Conference Papers*, pp. 1–11, 2024.
- Jiemin Fang, Taoran Yi, Xinggang Wang, Lingxi Xie, Xiaopeng Zhang, Wenyu Liu, Matthias Nießner, and Qi Tian. Fast dynamic radiance fields with time-aware neural voxels. In *SIGGRAPH Asia 2022 Conference Papers*, 2022.
- Sara Fridovich-Keil, Alex Yu, Matthew Tancik, Qinhong Chen, Benjamin Recht, and Angjoo Kanazawa. Plenoxels: Radiance fields without neural networks. In *Proceedings of the IEEE/CVF conference on computer vision and pattern recognition*, pp. 5501–5510, 2022.
- Sara Fridovich-Keil, Giacomo Meanti, Frederik Rahbæk Warburg, Benjamin Recht, and Angjoo Kanazawa. K-planes: Explicit radiance fields in space, time, and appearance. In *Proceedings of the IEEE/CVF Conference on Computer Vision and Pattern Recognition*, pp. 12479–12488, 2023.
- Zhiyang Guo, Wengang Zhou, Li Li, Min Wang, and Houqiang Li. Motion-aware 3d gaussian splatting for efficient dynamic scene reconstruction. *arXiv preprint arXiv:2403.11447*, 2024.
- Yi-Hua Huang, Yang-Tian Sun, Ziyi Yang, Xiaoyang Lyu, Yan-Pei Cao, and Xiaojuan Qi. Scgs: Sparse-controlled gaussian splatting for editable dynamic scenes. In *Proceedings of the IEEE/CVF Conference on Computer Vision and Pattern Recognition*, pp. 4220–4230, 2024.

- 540 Kai Katsumata, Duc Minh Vo, and Hideki Nakayama. A compact dynamic 3d gaussian representa-
541 tion for real-time dynamic view synthesis. In *ECCV*, 2024.
- 542
- 543 Bernhard Kerbl, Georgios Kopanas, Thomas Leimkühler, and George Drettakis. 3d gaussian splat-
544 ting for real-time radiance field rendering. *ACM Transactions on Graphics*, 42(4), July 2023.
545 URL <https://repo-sam.inria.fr/fungraph/3d-gaussian-splatting/>.
- 546 Diederik P Kingma. Adam: A method for stochastic optimization. *arXiv preprint arXiv:1412.6980*,
547 2014.
- 548
- 549 Julian Knodt. Continuous dynamic-nerf: Spline-nerf, 2022. URL [https://arxiv.org/abs/](https://arxiv.org/abs/2203.13800)
550 2203.13800.
- 551 Minsik Lee, Jungchan Cho, and Songhwai Oh. Consensus of non-rigid reconstructions. In *Pro-*
552 *ceedings of the IEEE Conference on Computer Vision and Pattern Recognition*, pp. 4670–4678,
553 2016.
- 554
- 555 Tianye Li, Mira Slavcheva, Michael Zollhoefer, Simon Green, Christoph Lassner, Changil Kim,
556 Tanner Schmidt, Steven Lovegrove, Michael Goesele, Richard Newcombe, et al. Neural 3d video
557 synthesis from multi-view video. In *Proceedings of the IEEE/CVF Conference on Computer*
558 *Vision and Pattern Recognition*, pp. 5521–5531, 2022.
- 559 Zhan Li, Zhang Chen, Zhong Li, and Yi Xu. Spacetime gaussian feature splatting for real-time
560 dynamic view synthesis. In *Proceedings of the IEEE/CVF Conference on Computer Vision and*
561 *Pattern Recognition*, pp. 8508–8520, 2024.
- 562
- 563 Youtian Lin, Zuozhuo Dai, Siyu Zhu, and Yao Yao. Gaussian-flow: 4d reconstruction with dynamic
564 3d gaussian particle. In *Proceedings of the IEEE/CVF Conference on Computer Vision and Pat-*
565 *tern Recognition*, pp. 21136–21145, 2024.
- 566
- 567 Qingming Liu, Yuan Liu, Jiepeng Wang, Xianqiang Lv, Peng Wang, Wenping Wang, and Junhui
568 Hou. Modgs: Dynamic gaussian splatting from causally-captured monocular videos. *arXiv*
preprint arXiv:2406.00434, 2024.
- 569 Zhicheng Lu, Xiang Guo, Le Hui, Tianrui Chen, Ming Yang, Xiao Tang, Feng Zhu, and Yuchao Dai.
570 3d geometry-aware deformable gaussian splatting for dynamic view synthesis. In *Proceedings of*
571 *the IEEE/CVF Conference on Computer Vision and Pattern Recognition*, 2024.
- 572
- 573 Jonathon Luiten, Georgios Kopanas, Bastian Leibe, and Deva Ramanan. Dynamic 3d gaussians:
574 Tracking by persistent dynamic view synthesis. In *3DV*, 2024.
- 575
- 576 Ben Mildenhall, Pratul P. Srinivasan, Matthew Tancik, Jonathan T. Barron, Ravi Ramamoorthi, and
577 Ren Ng. Nerf: Representing scenes as neural radiance fields for view synthesis. In *ECCV*, 2020.
- 578
- 579 Thomas Müller. `tiny-cuda-nn`, 4 2021. URL [https://github.com/NVlabs/](https://github.com/NVlabs/tiny-cuda-nn)
580 `tiny-cuda-nn`.
- 581
- 582 Thomas Müller, Alex Evans, Christoph Schied, and Alexander Keller. Instant neural graphics prim-
583 itives with a multiresolution hash encoding. *ACM transactions on graphics (TOG)*, 41(4):1–15,
584 2022.
- 585
- 586 Keunhong Park, Utkarsh Sinha, Jonathan T. Barron, Sofien Bouaziz, Dan B Goldman, Steven M.
587 Seitz, and Ricardo Martin-Brualla. Nerfies: Deformable neural radiance fields. *ICCV*, 2021a.
- 588
- 589 Keunhong Park, Utkarsh Sinha, Peter Hedman, Jonathan T. Barron, Sofien Bouaziz, Dan B Gold-
590 man, Ricardo Martin-Brualla, and Steven M. Seitz. Hypernerf: A higher-dimensional representa-
591 tion for topologically varying neural radiance fields. *ACM Trans. Graph.*, 40(6), dec 2021b.
- 592
- 593 Adam Paszke, Sam Gross, Francisco Massa, Adam Lerer, James Bradbury, Gregory Chanan,
594 Trevor Killeen, Zeming Lin, Natalia Gimelshein, Luca Antiga, Alban Desmaison, Andreas
595 Kopf, Edward Yang, Zachary DeVito, Martin Raison, Alykhan Tejani, Sasank Chilamkurthy,
596 Benoit Steiner, Lu Fang, Junjie Bai, and Soumith Chintala. Pytorch: An imperative style, high-
597 performance deep learning library. In *Advances in Neural Information Processing Systems* 32, pp.
598 8024–8035. Curran Associates, Inc., 2019. URL <http://papers.neurips.cc/paper/>

594 9015-pytorch-an-imperative-style-high-performance-deep-learning-library.
595 pdf.
596

597 Les Piegl and Wayne Tiller. *The NURBS book*. Springer Science & Business Media, 2012.

598 Albert Pumarola, Enric Corona, Gerard Pons-Moll, and Francesc Moreno-Noguer. D-nerf: Neural
599 radiance fields for dynamic scenes. In *Proceedings of the IEEE/CVF Conference on Computer
600 Vision and Pattern Recognition*, pp. 10318–10327, 2021.

601 Johannes L. Schönberger and Jan-Michael Frahm. Structure-from-motion revisited. In *2016 IEEE
602 Conference on Computer Vision and Pattern Recognition (CVPR)*, pp. 4104–4113, 2016. doi:
603 10.1109/CVPR.2016.445.
604

605 Liangchen Song, Anpei Chen, Zhong Li, Zhang Chen, Lele Chen, Junsong Yuan, Yi Xu, and An-
606 dreas Geiger. Nerfplayer: A streamable dynamic scene representation with decomposed neural
607 radiance fields. *IEEE Transactions on Visualization and Computer Graphics*, 29(5):2732–2742,
608 2023. doi: 10.1109/TVCG.2023.3247082.

609 Guanjun Wu, Taoran Yi, Jiemin Fang, Lingxi Xie, Xiaopeng Zhang, Wei Wei, Wenyu Liu, Qi Tian,
610 and Xinggang Wang. 4d gaussian splatting for real-time dynamic scene rendering. In *Proceedings
611 of the IEEE/CVF Conference on Computer Vision and Pattern Recognition (CVPR)*, pp. 20310–
612 20320, June 2024.

613 Zeyu Yang, Hongye Yang, Zijie Pan, and Li Zhang. Real-time photorealistic dynamic scene rep-
614 resentation and rendering with 4d gaussian splatting. In *International Conference on Learning
615 Representations (ICLR)*, 2024a.

616 Ziyi Yang, Xinyu Gao, Wen Zhou, Shaohui Jiao, Yuqing Zhang, and Xiaogang Jin. Deformable
617 3d gaussians for high-fidelity monocular dynamic scene reconstruction. In *Proceedings of the
618 IEEE/CVF Conference on Computer Vision and Pattern Recognition*, pp. 20331–20341, 2024b.

619 Alex Yu, Ruilong Li, Matthew Tancik, Hao Li, Ren Ng, and Angjoo Kanazawa. PlenOctrees for
620 real-time rendering of neural radiance fields. In *ICCV*, 2021.

621 Heng Yu, Joel Julian, Zoltán Á Milacski, Koichiro Niinuma, and László A Jeni. Cogs: Controllable
622 gaussian splatting. In *Proceedings of the IEEE/CVF Conference on Computer Vision and Pattern
623 Recognition*, pp. 21624–21633, 2024.

624 Matthias Zwicker, Hanspeter Pfister, Jeroen Van Baar, and Markus Gross. Ewa volume splatting. In
625 *Proceedings Visualization, 2001. VIS'01.*, pp. 29–538. IEEE, 2001.

626
627
628
629
630
631
632
633
634
635
636
637
638
639
640
641
642
643
644
645
646
647

APPENDIX

A EXCLUSION OF SCALE VARIATIONS IN SPLINEGS

SplineGS does not model the scale variations of Gaussian blobs. This can prohibit certain objects, such as jelly- or smoke-like structures. However, for most types of objects, their parts exhibit minimal scaling changes. It is also reported in the literature that most non-rigid deformations are likely rigid transforms at infinitesimal levels (Lee et al., 2016). This perspective is also adequate for Gaussian splatting, considering that the blobs represent some small parts forming the objects in the scene. Therefore, we concentrate on modeling deformations in positions and rotations only. In reality, modeling scale variations tend to induce overfitting in our experience due to the additional degrees of freedom. We believe that scaling variations should be addressed with careful consideration as a separate research focus.

B MORE RESULTS

Table 5 shows the per-scene attributes of SplineGS, such as training time, FPS, and number of blobs, for the D-NeRF and Neu3D datasets. Table 6 presents quantitative comparisons of PSNR and SSIM across all scenes in the D-NeRF dataset. In each scene, the proposed method achieves highly competitive results. Table 7 presents quantitative comparisons of LPIPS across all scenes in the D-NeRF dataset. Here, we can confirm that SplineGS also achieves the best LPIPS performance in most cases. Figure 5 shows a scatter plot comparing the number of blobs, FPS, training time, and PSNR of various methods for the D-NeRF dataset. Here, SplineGS has a high average FPS even though its average number of Gaussian blobs is relatively large compared to those of the other methods. This confirms that the core design of the proposed method is indeed quite efficient, and it still achieves high performance. As illustrated in Figure 6, our method produces more accurate renderings than existing approaches. Similarly, Table 8 shows the quantitative comparisons of PSNR and SSIM across five scenes in the Neu3D dataset. Notably, our model achieves the best average performance. Figure 7 provides the rendering results for every 75 frames. Table 9 presents a quantitative comparison of PSNR for three vrng scenes in the HyperNeRF (Park et al., 2021b) dataset. Similar to Neu3D, the HyperNeRF dataset provides real-world scenes. Here, SplineGS achieves performance comparable to other methods. A critical problem with the HyperNeRF dataset is that the provided camera pose information is not accurate. An additional camera pose optimization is required to handle this problem, which is another set of problems left as future work.

Table 5: **Per-scene attributes of SplineGS for the D-NeRF and Neu3D datasets.** We present the training time, FPS, and number of blobs for each scene. The number of representative trajectories L was $L = 64$ for *mutant* and *bouncing balls*, while that was $L = 128$ for the other scenes.

D-NeRF				Neu3D			
Scene	Time (min)	FPS	#Blobs	Scene	Time (min)	FPS	#Blobs
Trex	41	133	250K	Coffee Martini	67	62	386K
Jumping Jack	33	197	126K	Spinach	53	81	140K
Hell Warrior	28	263	52K	Cut Beef	52	79	167K
Stand Up	31	227	98K	Sear Steak	52	84	138K
Bouncing balls	38	176	167K	Flame Steak	50	76	143K
Mutant	34	192	165K				
Hook	33	186	161K				
Lego	42	133	320K				

Table 6: **Quantitative comparison for the D-NeRF dataset.** We compared our method to existing methods on 800×800 resolution test images. Here, “40K” and “80K” in the parentheses indicate the numbers of training iterations. The asterisks (*) indicate that the results were adopted from the 4D-GS paper (Wu et al., 2024), while the daggers (†) indicate that those were from the original papers. All the other results were reproduced in our experiments. The average PSNR and SSIM are measured across all scenes, with some cells highlighted to represent the **best**, **second best**, and **third best**.

Method	Trex		Jumping Jacks		Hell Warrior	
	PSNR↑	SSIM↑	PSNR↑	SSIM↑	PSNR↑	SSIM↑
K-Planes* (Fridovich-Keil et al., 2023)	30.43	0.9737	31.11	0.9708	24.58	0.9520
HexPlane* (Cao & Johnson, 2023)	30.67	0.9749	31.31	0.9729	24.55	0.9443
TiNeuVox* (Fang et al., 2022)	31.25	0.9666	33.49	0.9771	27.10	0.9638
D-3DGS† (Yang et al., 2024b)	38.10	0.9933	37.72	0.9897	41.54	0.9873
4D-GS* (Wu et al., 2024)	34.23	0.9850	35.42	0.9857	28.71	0.9733
4DGS (Yang et al., 2024a)	30.38	0.9743	32.10	0.9639	34.32	0.9536
CoGS† (Yu et al., 2024)	37.25	0.9923	37.48	0.9891	40.43	0.9812
NPGs† (Das et al., 2024)	32.10	0.9818	33.97	0.9828	38.68	0.9780
CompDynGS† (Katsumata et al., 2024)	28.17	0.9740	32.93	0.9840	35.36	0.9650
SC-GS (Huang et al., 2024)	39.61	0.9981	39.43	0.9964	42.20	0.9925
SplineGS (40K)	37.96	0.9925	38.29	0.9906	42.26	0.9890
SplineGS (80K)	38.77	0.9931	38.66	0.9908	42.52	0.9893
Method	Stand up		Bouncing Balls		Mutant	
	PSNR↑	SSIM↑	PSNR↑	SSIM↑	PSNR↑	SSIM↑
K-Planes* (Fridovich-Keil et al., 2023)	33.10	0.9793	40.05	0.9934	32.50	0.9713
HexPlane* (Cao & Johnson, 2023)	34.40	0.9839	39.86	0.9915	33.67	0.9802
TiNeuVox* (Fang et al., 2022)	34.61	0.9797	40.23	0.9926	30.87	0.9607
D-3DGS† (Yang et al., 2024b)	44.62	0.9951	41.01	0.9953	42.63	0.9951
4D-GS* (Wu et al., 2024)	38.11	0.9898	40.62	0.9942	37.59	0.9880
4DGS (Yang et al., 2024a)	38.83	0.9857	33.28	0.9842	37.43	0.9842
CoGS† (Yu et al., 2024)	43.35	0.9929	40.98	0.9958	42.14	0.9937
NPGs† (Das et al., 2024)	38.20	0.9889	-	-	36.02	0.9840
CompDynGS† (Katsumata et al., 2024)	40.21	0.9940	33.29	0.9840	38.04	0.9940
SC-GS (Huang et al., 2024)	46.47	0.9989	41.39	0.9960	43.42	0.9989
SplineGS (40K)	45.50	0.9940	41.71	0.9956	43.29	0.9960
SplineGS (80K)	46.00	0.9944	41.81	0.9956	43.73	0.9962
Method	Hook		Lego		Mean	
	PSNR↑	SSIM↑	PSNR↑	SSIM↑	PSNR↑	SSIM↑
K-Planes* (Fridovich-Keil et al., 2023)	28.12	0.9489	25.49	0.9483	30.67	0.9672
HexPlane* (Cao & Johnson, 2023)	28.63	0.9572	25.10	0.9388	31.02	0.9680
TiNeuVox* (Fang et al., 2022)	28.63	0.9433	24.65	0.9063	31.35	0.9613
D-3DGS† (Yang et al., 2024b)	37.42	0.9867	24.94	0.9432	38.50	0.9857
4D-GS* (Wu et al., 2024)	32.73	0.9760	25.03	0.9378	34.06	0.9787
4DGS (Yang et al., 2024a)	31.92	0.9546	24.70	0.9189	32.87	0.9649
CoGS† (Yu et al., 2024)	36.43	0.9838	25.16	0.9451	37.90	0.9842
NPGs† (Das et al., 2024)	33.39	0.9735	24.63	0.9312	-	-
CompDynGS† (Katsumata et al., 2024)	33.43	0.9810	24.26	0.9400	33.21	0.9770
SC-GS (Huang et al., 2024)	38.88	0.9956	24.92	0.9485	39.53	0.9906
SplineGS (40K)	38.61	0.9891	25.29	0.9457	39.11	0.9866
SplineGS (80K)	38.71	0.9891	25.29	0.9457	39.44	0.9868

Table 7: **LPIPS comparison for the D-NeRF dataset.** We compared our method to existing methods on 800×800 resolution images based on LPIPS. The daggers (\dagger) indicate that those were from the original papers.

Method	Trex	Jumping Jakcs	Hell Warrior
4D-GS \dagger	0.0131	0.0128	0.0369
D-3DGS \dagger	0.0098	0.0126	0.0234
SC-GS	0.0119	0.0115	0.0280
SplineGS	0.0047	0.0065	0.0091
Method	Stand up	Bouncing Balls	Mutant
4D-GS \dagger	0.0074	0.0155	0.0167
D-3DGS \dagger	0.0063	0.0093	0.0052
SC-GS	0.0072	0.0216	0.0069
SplineGS	0.0027	0.0025	0.0019
Method	Hook	Lego	Mean
4D-GS \dagger	0.0272	0.0382	0.0210
D-3DGS \dagger	0.0144	0.0183	0.0124
SC-GS	0.0139	0.0499	0.0119
SplineGS	0.0065	0.0298	0.0080

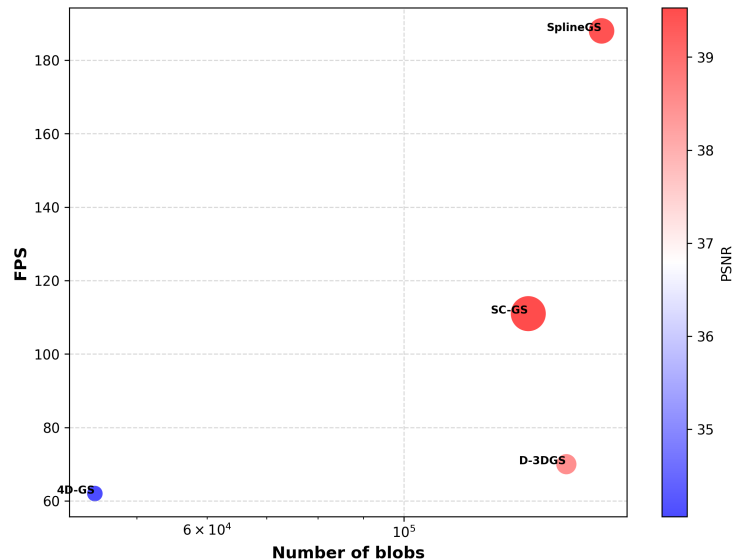


Figure 5: A scatter plot of various methods based on the number of blobs, FPS, training time, and PSNR. We compared SplineGS to existing methods on a scatter plot for the D-NeRF dataset. The x-axis represents the average number of blobs, and the y-axis represents the average FPS. The size of each circle indicates the average training time, while the color represents the average PSNR.

810
811
812
813
814
815
816
817
818
819
820
821
822
823
824
825
826
827
828
829
830
831
832
833
834
835
836
837
838
839
840
841
842
843
844
845
846
847
848
849
850
851
852
853
854
855
856
857
858
859
860
861
862
863

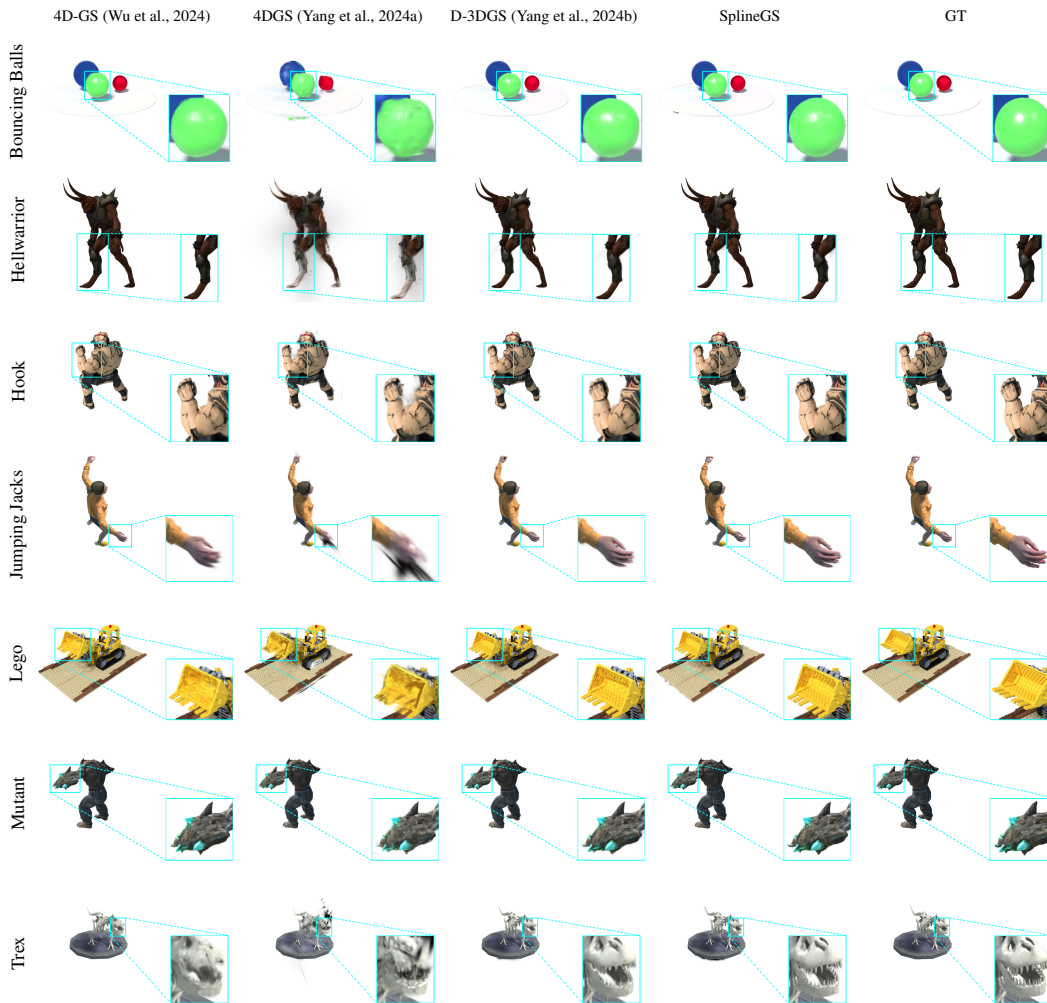


Figure 6: **Qualitative results on the D-NeRF dataset.** We present the rendering results of various methods, including ours, for all scenes in the D-NeRF dataset. The first to third columns show the results of existing methods, while the fourth and fifth columns show those of the proposed method and the ground truth, respectively. Each row shows the results of a different scene.

Table 8: **Quantitative comparison for the Neu3D dataset.** We compared our method with existing methods on 1352×1014 resolution test images. Here, “20K” and “40K” in the parentheses indicate the numbers of training iterations. The conventions for typographical marks and color codes are generally identical to Table 1. We measured the average PSNR and SSIM across all scenes except *flame_salmon*, following the practice of many existing works (Guo et al., 2024; Liu et al., 2024; Lu et al., 2024).

Method	Coffee Martini		Spinach		Cut Beef	
	PSNR↑	SSIM↑	PSNR↑	SSIM↑	PSNR↑	SSIM↑
NeRFPlayer* (Song et al., 2023)	32.05	0.9380	32.06	0.9300	31.83	0.9280
K-Planes* (Fridovich-Keil et al., 2023)	29.99	0.9530	32.60	0.9660	31.82	0.9660
HexPlane* (Cao & Johnson, 2023)	-	-	31.86	0.9830	32.71	0.9850
4D-GS* (Wu et al., 2024)	27.34	0.9050	32.46	0.9490	32.90	0.9570
4DGS† (Yang et al., 2024a)	28.33	-	32.93	-	33.85	0.9800
STG† (Li et al., 2024)	28.61	0.9585	33.18	0.9785	33.52	0.9795
SplineGS (20K)	29.16	0.9171	33.04	0.9538	33.42	0.9541
SplineGS (40K)	29.26	0.9189	33.09	0.9542	33.49	0.9544
Method	Sear Steak		Flame Steak		Mean	
	PSNR↑	SSIM↑	PSNR↑	SSIM↑	PSNR↑	SSIM↑
NeRFPlayer* (Song et al., 2023)	32.31	0.9400	27.36	0.8670	32.12	0.9206
K-Planes* (Fridovich-Keil et al., 2023)	32.52	0.9740	32.39	0.9700	31.86	0.9658
HexPlane* (Cao & Johnson, 2023)	32.09	0.9860	31.92	0.9880	-	-
4D-GS* (Wu et al., 2024)	32.49	0.9570	32.51	0.9540	31.54	0.9444
4DGS† (Yang et al., 2024a)	33.51	-	34.03	-	32.53	-
STG† (Li et al., 2024)	33.89	0.9826	33.64	0.9824	32.57	0.9740
SplineGS (20K)	33.75	0.9621	33.23	0.9578	32.52	0.9484
SplineGS (40K)	33.82	0.9624	33.33	0.9582	32.60	0.9496

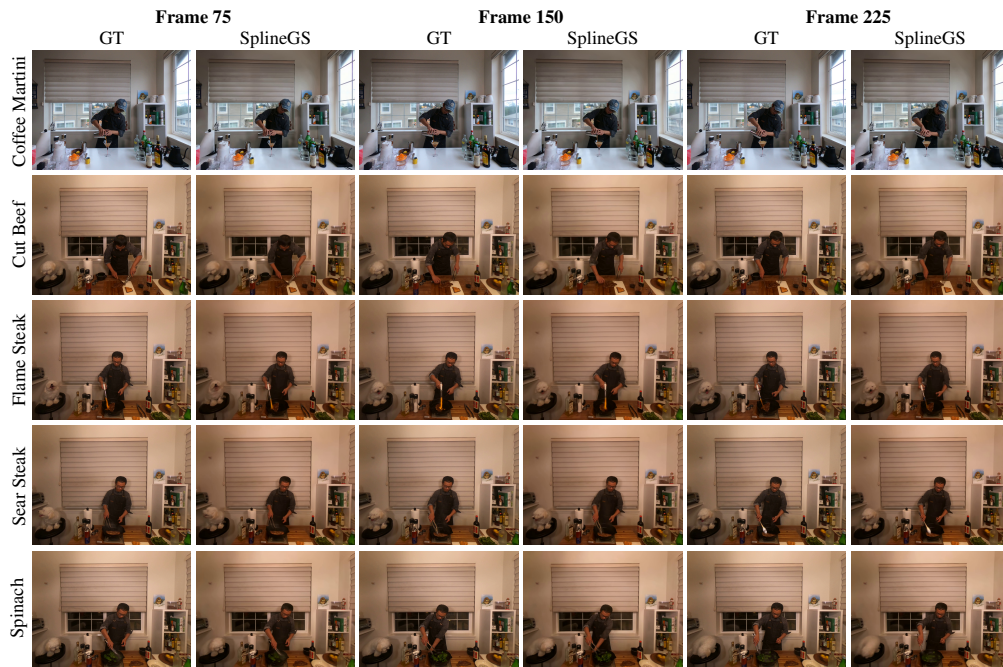


Figure 7: **Qualitative results on the Neu3D dataset.** We show the qualitative results of SplineGS on the Neu3D datasets except for *flame_salmon*. We provide the ground truth and the results of SplineGS for the 75th, 150th, and 225th frames. Each row shows the results of a different scene.

918
919
920
921
922
923
924
925
926
927
928
929
930
931
932
933
934
935
936
937
938
939
940
941
942
943
944
945
946
947
948
949
950
951
952
953
954
955
956
957
958
959
960
961
962
963
964
965
966
967
968
969
970
971

Table 9: **Quantitative comparison for the HyperNeRF dataset.** We compared our method to existing methods on half-resolution test images and measured PSNR for three vrig scenes. The daggers (†) indicate that those were from the original papers.

Method	3D Printer	Chicken	Broom
D-3DGS (Yang et al., 2024b)	20.28	22.76	20.47
4D-GS [†] (Wu et al., 2024)	22.10	28.70	22.00
SplineGS	21.97	29.13	20.56